

The High Temperature Strength of Single Crystal Ni-base Superalloys – Re-visiting Constant Strain Rate, Creep, and Thermomechanical Fatigue Testing

Marc Sirrenberg,* Tomáš Babinský, David Bürger, Stefan Guth, Alireza B. Parsa, Pascal Thome, Antonín Dlouhý, Michael J. Mills, and Gunther Eggeler

The present work takes a new look at the high temperature strength of single crystal (SX) Ni-base superalloys. It compares high temperature constant strain rate (CSR) testing, creep testing, and out-of-phase thermomechanical fatigue (OP-TMF) testing, which represent key characterization methods supporting alloy development and component design in SX material science and technology. The three types of tests are compared using the same SX alloy, working with precisely oriented $\langle 001 \rangle$ -specimens and considering the same temperature range between 1023 and 1223 K, where climb controlled micro-creep processes need to be considered. Nevertheless, the three types of tests provide different types of information. CSR testing at imposed strain rates of $3.3 \times 10^{-4} \text{ s}^{-1}$ shows a yield stress anomaly (YSA) with a YSA stress peak at a temperature of 1073 K. This increase of strength with increasing temperature is not observed during constant load creep testing at much lower deformation rates around 10^{-7} s^{-1} . Creep rates show a usual behavior and increase with increasing temperatures. During OP-TMF loading, the temperature continuously increases/decreases in the compression/tension part of the mechanical strain-controlled cycle ($\pm 0.5\%$). At the temperature, where the YSA peak stress temperature is observed, no peculiarities are observed. It is shown that OP-TMF life is sensitive to surface quality, which is not the case in creep. A smaller number of cycles to failure is observed when reducing the heating rate in the compression/heating part of the mechanical strain-controlled OP-TMF cycle. The results are discussed on a microstructural basis, using results from scanning and transmission electron microscopy, and in light of previous work published in the literature.

1. Introduction

Ni-base single crystal superalloys (SXs) are used to make blades for gas turbines operating in aero engines and powerplants (e.g., refs. [1–6]). These components are exposed to static and cyclic mechanical loads at temperatures close to their melting point. The high temperature strength of a material represents its resistance against a change in shape and rupture. The mechanical load spectrum of a high temperature SX turbine blade is complex. Creep is important but fatigue loading also plays a crucial role. Since cyclic loading is often associated with start-up and shut-off events, anisothermal thermomechanical fatigue (TMF) behavior is of interest. Micro-creep processes contribute to high temperature plasticity in all three cases.

In the laboratory, SX behavior is characterized in different types of experiments. High temperature constant strain rate (CSR) tensile testing is probably the most widely used standard characterization method (e.g., refs. [7–11]). Creep^[12–16] and TMF testing^[17–21] are more relevant regarding the exploitable component life and both test methods are therefore important. Thermal fatigue loading is associated

M. Sirrenberg, D. Bürger, A. B. Parsa, G. Eggeler
Institut für Werkstoffe
Ruhr-Universität Bochum
Universitätsstr. 150, 44801 Bochum, Germany
E-mail: marc.sirrenberg@rub.de

T. Babinský, A. Dlouhý
Institute of Physics of Materials
Czech Academy of Sciences
Žitkova 513/22, 61600 Brno, Czech Republic

S. Guth
Institut für Angewandte Materialien – Werkstoffkunde
Karlsruher Institut für Technologie
Engelbert-Arnold-Straße 4, 76131 Karlsruhe, Germany

P. Thome
Department of Materials Science and Engineering
The University of Arizona
Tucson, AZ 85721-0012, USA

M. J. Mills
Materials Science and Engineering Department
The Ohio State University
2041 College Road, Columbus, OH 43210-1178, USA

 The ORCID identification number(s) for the author(s) of this article can be found under <https://doi.org/10.1002/adem.202400368>.

© 2024 The Author(s). Advanced Engineering Materials published by Wiley-VCH GmbH. This is an open access article under the terms of the Creative Commons Attribution-NonCommercial-NoDerivs License, which permits use and distribution in any medium, provided the original work is properly cited, the use is non-commercial and no modifications or adaptations are made.

DOI: 10.1002/adem.202400368

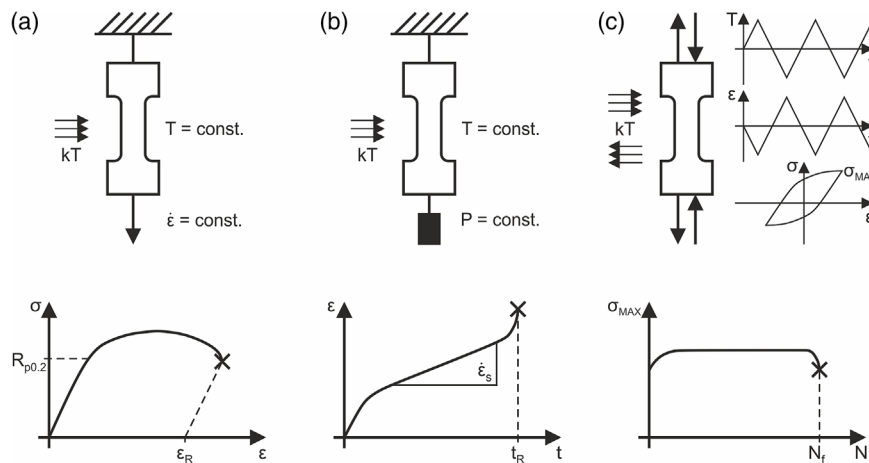


Figure 1. Schematic illustration of high temperature tests and examples for idealized test results. a) Constant strain rate (CSR) testing ($T = \text{const.}$, $\dot{\epsilon} = \text{const.}$) and stress–strain $\sigma(\epsilon)$ curve. b) Creep testing and creep $\epsilon(t)$ curve. c) Anisothermal out-of-phase thermomechanical fatigue (OP-TMF) testing and σ_{MAX} vs. N curve.

with start-up and shut-off events, where imposed thermal stresses and variable temperatures increase and decrease with a phase shift. This is why there is an interest in out-of-phase thermomechanical fatigue loading (OP-TMF).

In CSR testing, as constant strain rate is imposed on a specimen and the resulting stress–strain response is recorded, **Figure 1a**. From the resulting stress–strain curve an apparent critical yield stress $R_{p0.2}$ is retrieved. It is relatively simple to perform a CSR test. In contrast, creep and OP-TMF testing are more complex. During tensile creep, a specimen is subjected to a constant stress and the accumulation of strain with time is measured. The results yield creep curves as shown in **Figure 1b**, which directly provide information on times needed to obtain critical strain levels, rupture ductilities and rupture times t_R . When creep data are available for different stresses and temperatures, one can derive the stress and temperature dependencies of minimum creep rates $\dot{\epsilon}_s$ and rupture times t_R . In TMF testing, a solid round specimen is subjected to strain-controlled tension compression loading. Simultaneously the test temperatures vary between a low and a high temperature. In out-of-phase TMF testing, temperatures decrease as strains simultaneously increase and vice versa, **Figure 1c**. TMF results are typically presented as stress–strain hysteresis loops for different cycle numbers or as the evolution of stresses, e.g., maximum stress σ_{MAX} as a function of the cycle number N . They also yield the number of cycles to failure N_f for a given TMF loading condition.

Research on high temperature strength of SXs often focusses on only one of these three loading types. A critical comparison of the three types of tests, performed with the same material in the same temperature range is presently missing. This is the starting point of the present work, where we first explore CSR and creep behavior at temperatures ranging from 1023 to 1223 K, and then perform out-of-phase TMF testing with 1023–1223 K as minimum (T_{MIN}) and maximum (T_{MAX}) temperatures.

There is an uncertainty with some of the previous work published in the literature which is associated with specimen orientation. In SX technology one strives for $\langle 100 \rangle$

orientations.^[1,5,22,23] However, variation of the order of several degrees from this targeted growth direction cannot be easily avoided and are generally accepted.^[5] This, however, can cause severe deviations in the mechanical behavior, as has been recently shown by Heep et al.^[24] for creep testing. In the present work we use a combined Laue/spark erosion technique to manufacture precisely oriented CSR, creep, and TMF specimens (precision: $\langle 100 \rangle \pm 1^\circ$).

During high temperature exposure the cuboidal microstructure of SX, characterized by cuboidal γ' -particles (L1₂ phase, typical average volume fraction: 65%, typical average edge length: 400 nm) which are separated by thin γ -channels (fcc crystal structure, typical average volume fraction: 35%, average channel width: 50 nm) evolves. Rafting and topological inversion are well-known phenomena.^[25–40] In laboratory time scales, these processes manifest themselves at temperatures above 1173 K and are fast above 1273 K. The maximum temperature of 1223 K was chosen, to allow this type of microstructural evolution during the duration of the mechanical test. The present work represents the first attempt to compare the behavior of one batch of a single crystal Ni-base superalloy in three important mechanical tests in the same temperature range and with precisely oriented specimens. High temperature components have to withstand creep and OP-TMF loading and there is a need to consider possible interactions between these loading modes. Creep testing, CSR testing, and OP-TMF testing of superalloys are important topics with their own specialized scientific communities. The present work intends to bridge the gaps between these fields.

2. Experimental Section

2.1. Material

The Ni-base single crystal superalloy investigated in the present work is an alloy of CMSX-4 type, referred to as ERBO/1. Its chemical composition and its heat treatment are given elsewhere.^[41] Experimental details of the directional solidification

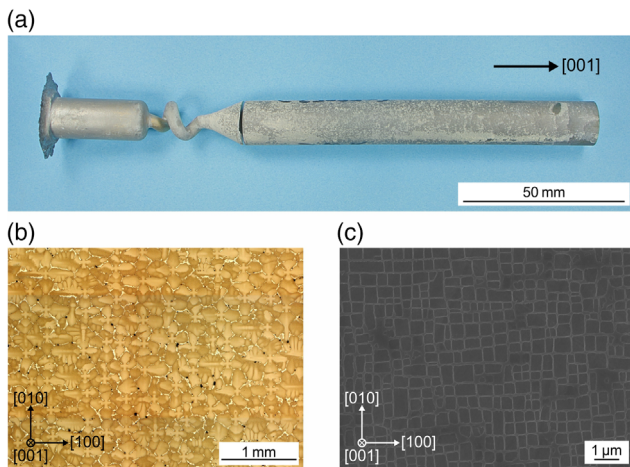


Figure 2. Material investigated in the present study. a) Image of directionally solidified cylinder (diameter: 20 mm). b) Optical micrograph of prior dendrites and interdendritic regions. c) SEM micrograph of γ/γ' -microstructure.

process^[42] and the details of the heat treatment procedure^[43] have been described elsewhere. The as cast cylindrical rod from which the specimens were machined is shown in **Figure 2a**. After the full heat treatment, traces of the prior dendritic/interdendritic microstructure can still be recognized,^[42,44] **Figure 2b**. The initial γ/γ' -microstructure of the material investigated in the present work is shown in **Figure 2c**. In the present work two types of surface qualities were considered, which are referred to as rough and smooth (as machined and polished). The surface qualities were characterized measuring surface roughness profiles with a laser scanning confocal microscope of type μ surf from NanoFocus. From the surface profiles, the roughness parameters R_a (mean value of height deviations from average height) and R_z (maximum peak to valley difference in the profile) were determined.^[45] The rougher surface was characterized by R_a/R_z -values of 0.43 and 3.43, respectively. For the polished surface these values were obtained as $R_a = 0.06$ and $R_z = 0.65$.

2.2. Test Rigs and Specimen Geometries

The three types of tests which are considered in the present work, are typically performed using different test rig configurations and different specimen geometries. This is illustrated in **Figure 3** and **4**. **Figure 3** shows the specimens as mounted in the respective test rigs prior to testing. The heating of the specimens during CSR and creep testing is performed using three-zone resistance furnaces. In the case of the OP-TMF testing, it was performed using induction heating.

The specimen geometries used for testing are shown in **Figure 4** at a higher magnification. It is important to highlight that in case of all three specimens, the diameters (CSR: 3 mm; TMF: 5 mm) and the two sides of the cross section of the miniature tensile creep specimen (MTC: $2 \times 3 \text{ mm}^2$) are larger than the average distance between the dendrites shown in **Figure 2b** (average distance between dendrites: 0.5 mm). Hence, the specimens yield properties which average over the large-scale microstructural cast heterogeneity leading to moderate variations in local stresses.^[46]

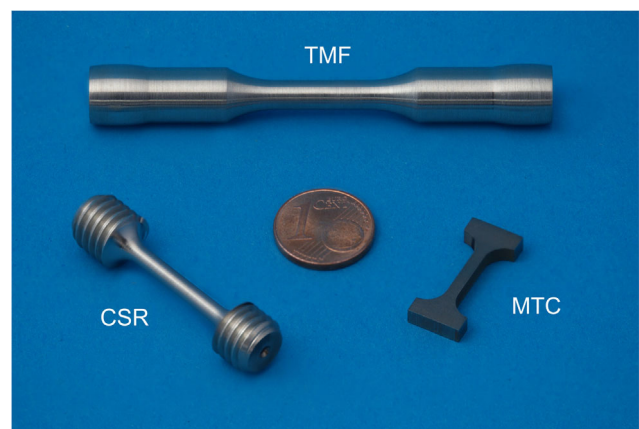


Figure 4. CSR-, creep- and OP-TMF specimens used for testing in the present work.

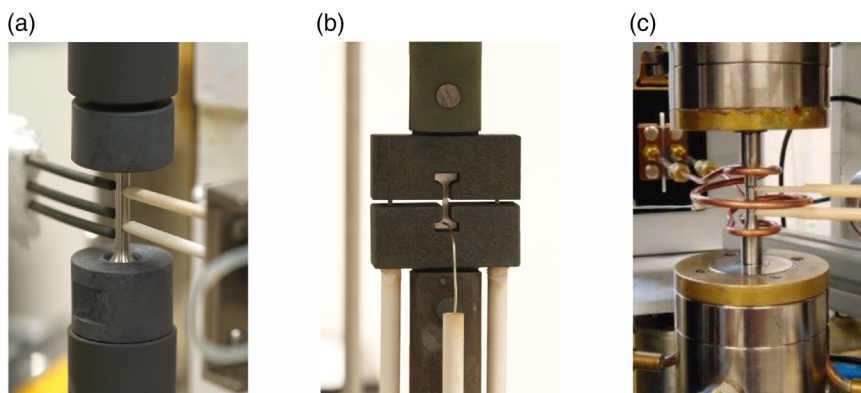


Figure 3. Specimens mounted in the load line of test rigs. a) CSR test rig MTS Criterion Model C45.105. For test details see.^[48] b) Creep machine from Denison Mayes type TC 20 Mark II. For test details see.^[49] c) Zwick 1478 Servo electric TMF test rig. For test details see.^[21]

2.3. CSR Testing

CSR tests were performed using an electromechanical test rig of type Criterion Model C45.105 from MTS, equipped with a three-zone resistance furnace. Figure 3a shows how the CSR specimen is mounted in the load line of the test rig. The specimen geometry is shown on the lower left of Figure 4. Strains were measured using a high temperature extensometer, where the tips of two ceramic rods were slightly pushed against the gauge length l_0 of 12 mm of the CSR specimen (two white ceramic rods in Figure 3a contacting the specimen from the right). From measured displacements Δl engineering strains ϵ_0 were obtained from which true strains ϵ were calculated^[47]

$$\epsilon_0 = \Delta l / l_0, \quad \epsilon = \ln(1 + \epsilon_0) \quad (1)$$

Tests were performed at temperatures between 1023 and 1223 K imposing strain rates between 8.0×10^{-5} and $1.3 \times 10^{-3} \text{ s}^{-1}$. The majority of CSR tests were performed at $3.3 \times 10^{-4} \text{ s}^{-1}$. More details of CSR testing are given elsewhere.^[48] Two characteristic stress values were determined: the apparent yield stress $R_{p0.2}$, Figure 5a and the stress measured after 2% CSR strain,

which is referred to as plateau stress σ_{PLATEAU} in the present work.

2.4. Creep Testing

Creep tests were performed at temperatures between 1023 and 1223 K at stresses ranging from 400 to 800 MPa. Figure 3b shows how the miniature creep specimen used in the present work was mounted in the load line of the test rig. The miniature creep specimen is shown at a higher magnification on the lower right of Figure 4. Details on how the specimens were heated, how loads were applied, and how strains were monitored are published in the literature.^[49] In the present work we perform isothermal creep tests and temperature change experiments as described by Bürger et al.^[50] In this study, creep curves are presented as log-linear plots of creep rates versus strain.

2.5. Thermomechanical Fatigue Testing

OP-TMF testing was performed in air on a servo electric mechanical test rig of type Zwick 1478 under total strain control. Heating

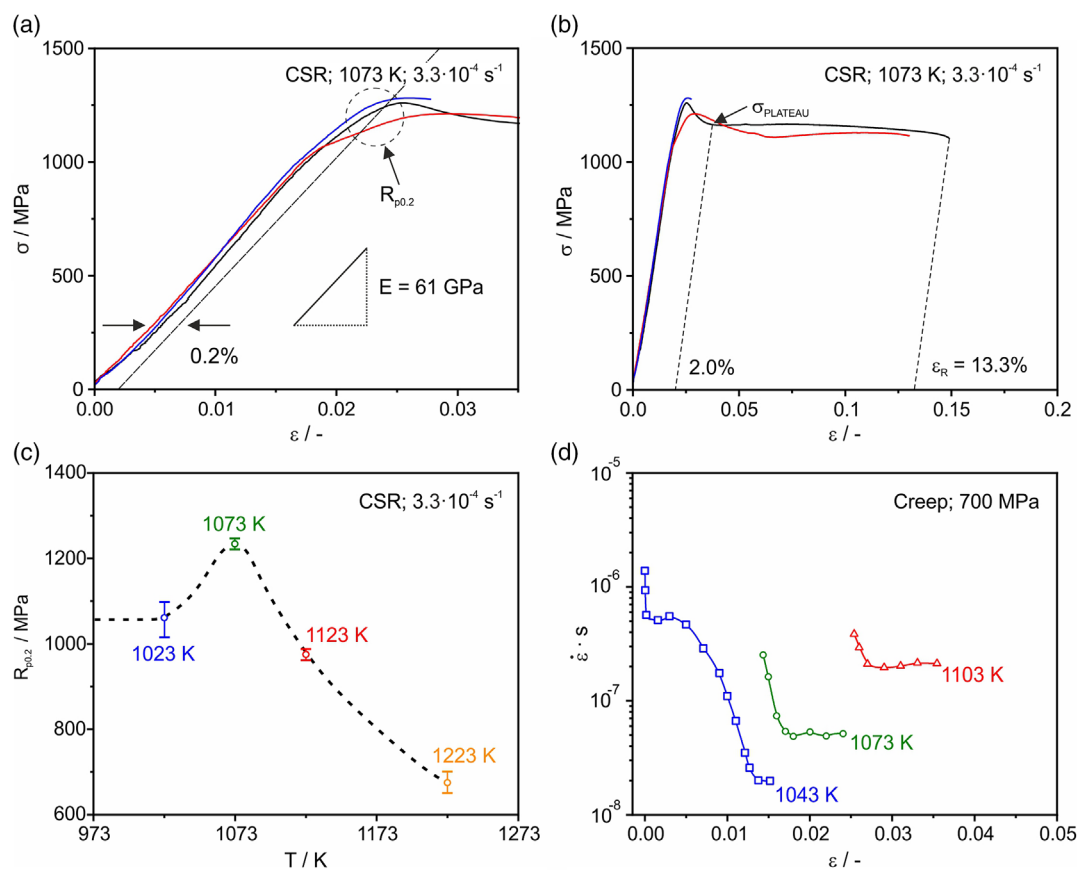


Figure 5. Results from CSR and creep tests. a) Stress–strain curve measured at 1073 K at a strain rate of $3.3 \times 10^{-4} \text{ s}^{-1}$ – early part of curve (high strain resolution). The intersection of the straight line in 0.2% distance from and parallel to the line of elastic loading with the experimental curves yields $R_{p0.2}$ values. b) Stress–strain curve measured at 1073 K at a strain rate of $3.3 \times 10^{-4} \text{ s}^{-1}$ – full curve (lower strain resolution). Plateau stresses were obtained from the intersections the straight line in 2% distance from and parallel to the line of elastic loading with the experimental curves. c) Yield stress anomaly (YSA)^[54–56] and subsequent decrease of yield stress as observed during CSR testing at temperatures between 1023 and 1223 K.^[48] d) Increase of creep rate with increasing temperature in the temperature range where CSR tests show YSA.^[48]

was realized via induction heating with water cooled copper coils (in the compression heating part of the cycle). Cooling (in the tension cooling part of the cycle) was achieved by thermal conduction to the water-cooled grips. Imposed strains and temperatures were out-of-phase, i.e., the maximum tensile strain of the stress–strain hysteresis loop was reached at the lowest temperature, while the maximum value of the compressive strain was reached at the highest temperature. Figure 3c shows the specimen in the central part of the TMF test rig, the TMF specimen as mounted in the test rig is shown in the upper part of Figure 4. Maximum and minimum temperatures during OP-TMF testing were 1023–1223 K. A total mechanical strain amplitude of 0.5% was imposed in all tests. Two types of heating/cooling cycles were compared. In both types of experiments, the cooling part of the cycle had a duration of 30 s (cooling rate for all tests: 6.66 K s^{-1} , total strain rate: $3.33 \times 10^{-4} \text{ s}^{-1}$). The two tests differed in the imposed heating rates which were fast (duration of heating period: 60 s, heating rate: 3.33 K s^{-1} , strain rate: $1.66 \times 10^{-4} \text{ s}^{-1}$) and slow (duration of heating period: 300 s, heating rate: 0.66 K s^{-1} , strain rate: $3.33 \times 10^{-5} \text{ s}^{-1}$). All details regarding OP-TMF testing are published elsewhere.^[51]

2.6. Characterization of Microstructures

Microstructural investigations were performed using a SEM of type Leo Gemini 1530 VP from Carl Zeiss AG and a transmission electron microscope (TEM) of type FEI Tecnai F20 G2 Super-Twin, following procedures which have been documented in the literature.^[37,38,46]

3. Results

3.1. CSR and Creep Results

Figure 5 compiles results from CSR tests. Figure 5a,b show stress–strain data which were obtained at 1073 K for an imposed deformation rate $\dot{\epsilon}_{\text{IMPOSED}}$ of $3.3 \times 10^{-4} \text{ s}^{-1}$ (test durations: 10–30 min) at a higher and lower strain resolution, respectively. Figure 5a shows that there is a linear increase of the stress–strain curve which yields an apparent elastic modulus of 61 GPa. Figure 5a also

shows how the apparent yield stress $R_{p0.2}$ was determined. Figure 5b shows that the CSR test at 1073 K yields a rupture strain of 13.3%. In Figure 5c apparent yield stress values from CSR experiments are shown, which were measured at four temperatures. Between 2 and 4 tests were performed for each temperature. The error bars in Figure 5c represent the \pm mean deviations from the mean value. Figure 5c clearly shows that starting at 1023 K, the engineering yield stress $R_{p0.2}$ increases, reaches a local maximum at 1073 K and then decreases. This represents experimental evidence for a yield stress anomaly (YSA) at lower/intermediate temperatures. Above the YSA peak, this anomaly is no longer detected and yield stresses decrease with increasing temperature. Under creep conditions, at much lower deformation rates, there is no increase of strength with increasing temperature where CSR tests exhibit YSA, Figure 5d. Instead, creep rates increase with increasing temperature.

Figure 6 shows CSR and creep results which were obtained at 1223 K, at temperatures far beyond the temperature of the yield stress maximum (1073 K). Figure 6a shows the stress–strain curves of three CSR experiments performed at different imposed strain rates. For CSR strain rates of 8.0×10^{-5} , 3.3×10^{-4} and $1.3 \times 10^{-3} \text{ s}^{-1}$, increasing plateau stresses (CSR stress values after 2%) of 761, 836, and 906 MPa were observed. Figure 6b shows creep results from isothermal creep tests. Creep curves obtained from experiments performed at 420, 550, and 680 MPa are presented as logarithmic strain rate as a function of strain. The corresponding minimum creep rates were determined as 1.32×10^{-7} , 2.02×10^{-6} , and $1.96 \times 10^{-5} \text{ s}^{-1}$. In Figure 6c the two stress/strain rate data triplets are plotted as logarithmic strain rate as a function of stress (Norton plot with creep and CSR data). It can be seen that the two data triplets can be fitted by straight lines which yield Norton stress exponents of 10 (creep data) and 16 (CSR data). The data, which are associated with a wide stress interval between 400 and 1000 MPa fall reasonably well into a small grey scatter band, with a slope of 12.

3.2. TMF Behavior

Figure 7 shows stress–strain hysteresis loops measured after 500 cycles. Figure 7a shows the stress–strain data recorded for the

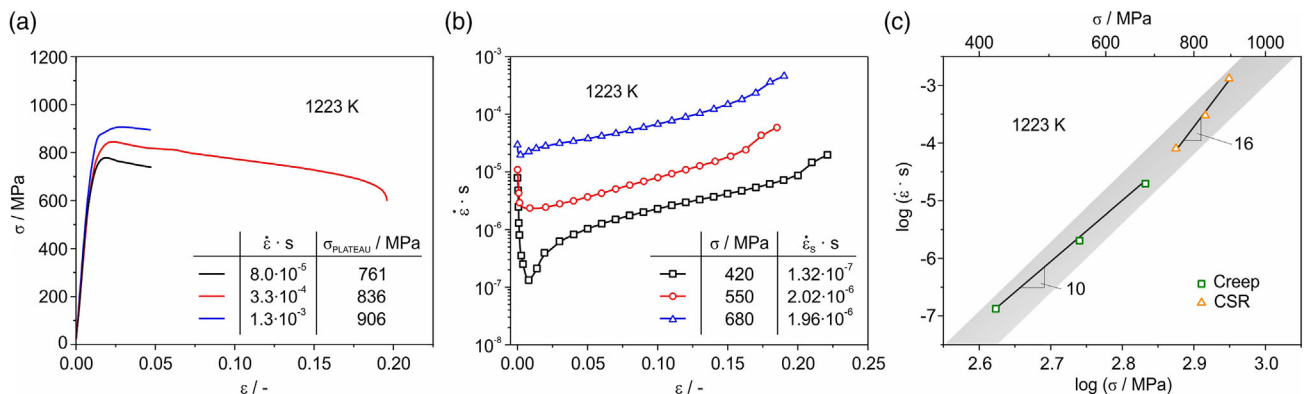


Figure 6. Results from CSR and creep tests obtained at 1223 K. a) Increase of $R_{p0.2}$ and plateau stress values with increasing imposed deformation rate. b) Log-linear plot of strain rates versus strain from creep tests performed at 420, 550 and 680 MPa. (b) Stress-strain curves from CSR tests performed at strain rates of 8.0×10^{-5} , 3.3×10^{-4} and $1.3 \times 10^{-3} \text{ s}^{-1}$. c) Stress/strain rate data triplets from creep and CSR tests in Norton plot. For details see text.

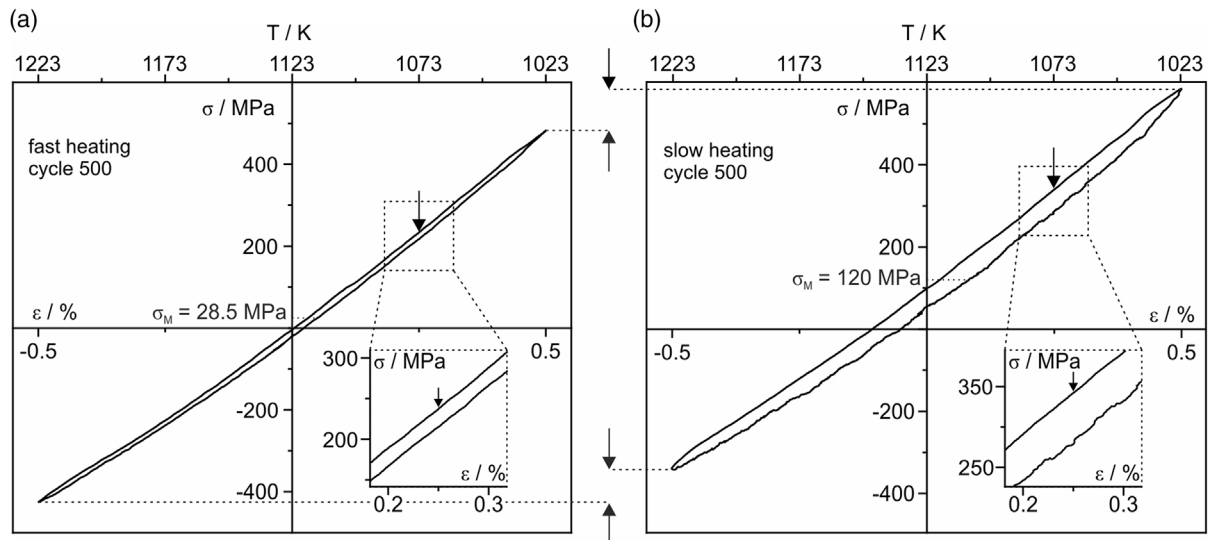


Figure 7. Stress-strain hysteresis loops recorded for cycle numbers 500 measured for an imposed mechanical strain of $\pm 0.5\%$ between 1023 K (minimum temperature in tensile part of cycle) and 1223 K (maximum temperature in compression part of cycle). Tensile cooling period: 30 s. a) Loop recorded for fast compression heating (60 s). b) Loop recorded for slow compression heating (300 s).

OP-TMF test with fast compression heating. The stress–strain hysteresis loop shown in Figure 7b was obtained for the OP-TMF conditions, with the same cooling rate but a five times longer compression heating period (300 s as compared to 60 s). For clarity, a number of details which are characteristic for anisothermal TMF testing must be highlighted. First, the absolute value of the saturation stress in tension (σ_{MAX} , lowest cycle temperature) is higher than in compression (σ_{MIN} , highest cycle temperature). Second, the TMF conditions imposed in the present work result in very narrow stress–strain hysteresis loop. However, one can clearly see that the area of the stress–strain hysteresis loop for fast heating (cycle shown in Figure 7a) is smaller ($\oint \sigma d\epsilon = 0.15 \text{ MJ m}^{-3}$) than for slow heating (cycle shown in Figure 7b), where more energy is dissipated ($\oint \sigma d\epsilon = 0.43 \text{ MJ m}^{-3}$). Finally, the origin of the co-ordinate system does not fall into the area of the hysteresis loops. During fast heating (cycle shown in Figure 7a) followed by fast cooling, the tensile loading at 482 MPa and 1023 K causes small (but detectable) positive plastic strain accumulation, which is not reversed in the heating cycle. In contrast, during slow heating (cycle shown in Figure 7b) there is significant compressive strain accumulation. This corresponds to a stronger relaxation of the absolute value of the compressive stress, which is lower than during fast heating (344 MPa as compared to 425 MPa). Figure 7 also shows that the OP-TMF experiment with fast compression heating has a lower positive mean stress in the cycle than the experiment with slow compression heating. Small vertical arrows in Figure 7a,b point to the stress–strain curves in the tensile cooling part of the cycles, where the temperature (1073 K) corresponds to the YSA peak temperature shown 5c. The OP-TMF stress–strain hysteresis loop does not show any peculiarities in this temperature region.

Figure 8a shows the evolution of the maximum tensile stresses in the cooling part of the cycle recorded for specimens

with rough and smooth surfaces. The stress response of the two specimens is slightly different although the same nominal strain amplitude was applied. Reasons for this may be slight deviations in thermal strain compensation. But even though the specimen with the rougher surface is exposed to lower maximum tensile stresses in the cold tensile part of the OP-TMF cycle, its failure occurs significantly earlier ($N_{f,RS} = 2122$) than the failure of the polished specimen ($N_{f,PS} = 5500$). This strong sensitivity of OP-TMF is not observed during creep testing at 1223 K/400 MPa, where specimens with rough and smooth surfaces yield very similar creep behavior, Figure 8b. The creep rupture time of the specimen with the rough surface was even a little larger than that of the polished creep specimen (81 and 76 h, respectively).

OP-TMF loading is associated with crack initiation and growth. Figure 9 shows cracks which are observed after 1000 slow compression heating OP-TMF cycles, imposed on specimens with smooth surfaces. Figure 9a shows circumferential surface cracks. Only a few of those grow into the material, as can be seen in Figure 9b, which shows that during OP-TMF a reaction layer forms that consists of an outer oxide and an inner γ' -depleted zone. This reaction layer is thicker in surface regions not affected by the presence of the crack. Along the crack flanks, its thickness increases from the crack tip to the outside, reflecting the effect of increasing exposure times. A small crack in the oxide is highlighted by a white arrow. It seems reasonable to assume that OP-TMF fatigue crack initiation started at this location.

It is also interesting to see that there is an indirect effect of creep on the cyclic OP-TMF lives, Figure 10. Figure 10 presents results which were obtained in OP-TMF tests with constant cooling rates in the tensile part of the cycles and fast and slow heating rates in the compression part of the cycle. The shapes of the imposed cycles are shown in Figure 10a,b. Tests were performed for smooth and rough specimen surfaces. Two results are presented in Figure 10c. First, the experiments with slow

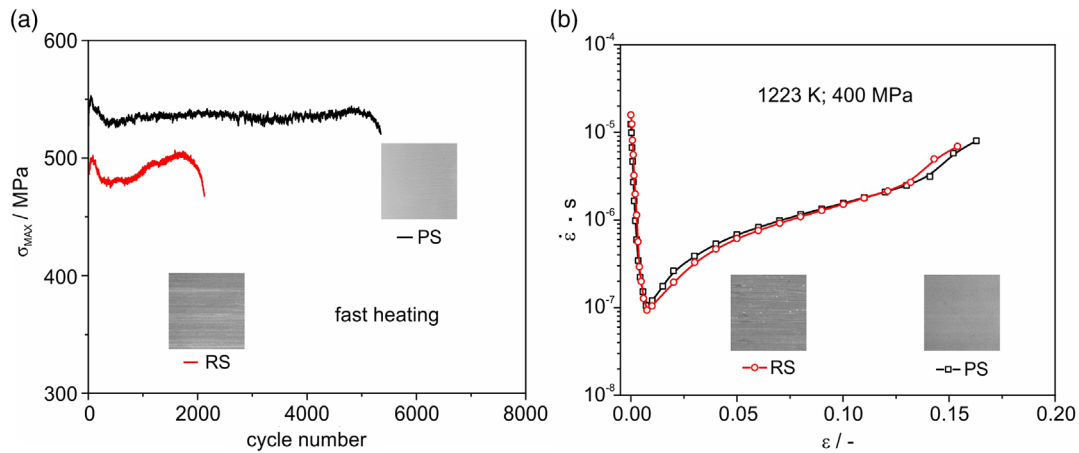


Figure 8. Sensitivity of TMF and creep behavior to surface roughness. All results were obtained for a material state with medium particle size. a) TMF results for rough and polished specimens from tests with fast heating during the compression part of the cycle (Figure 7a). b) Log-linear plots of creep rates versus strain for creep conditions of 1223 K and 400 MPa.

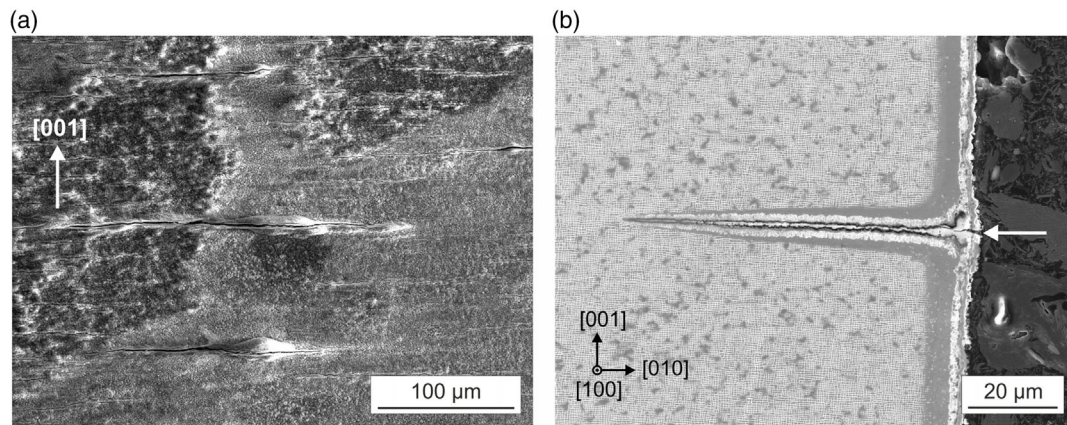


Figure 9. SEM results after 1000 slow compression heating OP-TMF cycles imposed on a specimen with a smooth surface. a) Circumferential cracks in the specimen surface. b) Macro crack observed in a longitudinal cross section.

compression heating cycles fail earlier than those where the periods of compression heating are shorter. Second, specimens with rough surfaces fail earlier than specimens with smooth surfaces.

3.3. TEM Micrographs

While a detailed TEM analysis is not in the scope of the present article, three typical TEM micrographs are shown in **Figure 11**, which were taken from cross sections perpendicular to the direction of the applied stress (parallel to [001]) after high temperature testing. Figure 11a shows a CSR microstructure which has evolved during a test performed with an imposed strain rate of $3.3 \times 10^{-4} \text{ s}^{-1}$ at the YSA peak temperature of 1073 K. The cuboidal γ' -particles show a darker contrast than the narrow γ -channels. Two microstructural features can be identified in the γ' -particles. There are planar faults which extend over more than one particle (two faults are identified with a white arrow pointing to the upper left). In addition, there are smaller features, which are Kear–Wilsdorf (KW) locks (two of which are highlighted with small white arrows pointing down).

Figure 11b shows a TEM microstructure which has evolved during 2% of creep at 1073 K, at a creep rate a little below 10^{-7} s^{-1} , Figure 5d. One can see that some coarsening has occurred, the γ -channels are wider than in Figure 11a. There are regions with a high density of dislocations (two marked with white arrows pointing down). One can also see planar faults extending over more than one γ' -particles (one highlighted with a white arrow pointing to the lower left). Figure 11c shows TEM results obtained after 4% high temperature and low stress creep (1223 K, 400 MPa). The γ/γ' -microstructure has evolved, two rafted γ' -particles are highlighted with a white arrow in the lower right of the image. An irregular dislocation network extends over a large part of the micrograph. The network is embedded in a horizontal γ -phase channel perpendicular to the direction of the applied stress. One can also distinguish cutting processes where individual superdislocations in the γ' -phase are connected to the γ -channel dislocation networks (two highlighted with horizontal white arrows). Figure 11 illustrates that significantly different microstructures evolved during CSR testing, low temperature high stress and high temperature low stress creep testing.

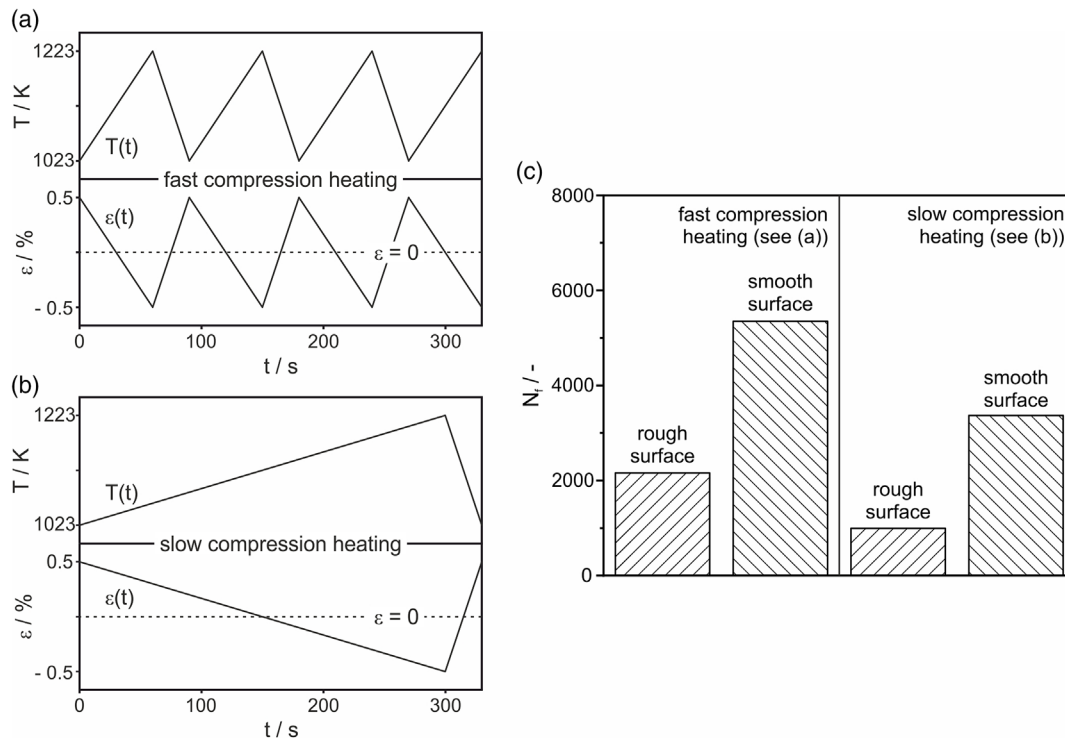


Figure 10. Influence of cycle type and surface roughness on cyclic mechanical strain-controlled ($\pm 0.5\%$) OP-TMF lives. a) Cycle shape where compression heating is fast. b) Cycle shape where compression heating is slow. c) Numbers of cycles to failure N_f for fast/slow compression heating and rough/smooth specimen surfaces. For details see text.

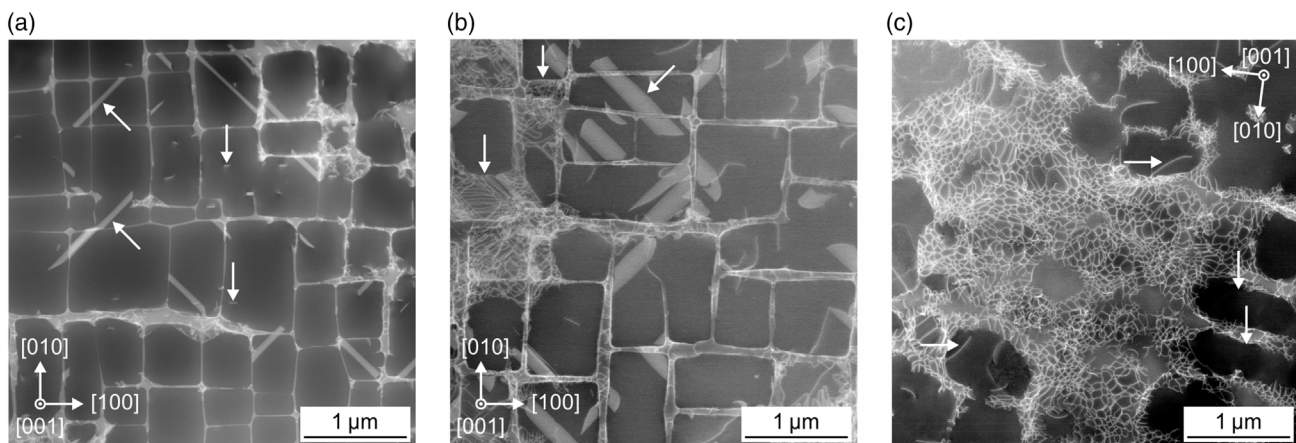


Figure 11. TEM micrographs from thin foils which were cut out perpendicular to the direction of the applied stress. a) After CSR testing: 1073 K / $3.3 \times 10^{-4} \text{ s}^{-1}$. b) After low temperature and high stress creep testing: 1073 K / 800 MPa. c) After high temperature and low stress creep testing: 1223 K / 400 MPa.

4. Discussion

4.1. Specimen Geometries

The mechanical results obtained in the present study were obtained using three different specimen geometries, Figure 3 and 4. All specimen dimensions were significantly larger than critical microstructural distances and there are no size effects, which need to be considered. In principle, when reporting

stresses (force normalized by cross section) and strains (elongations normalized by initial length) geometrical aspects are taken care of. However, as pointed out in the excellent review by Skrotzki et al.^[52] performing mechanical tests at high temperatures can be complex. Compared to room temperature testing, additional phenomena, like time-dependent deformation processes and oxidation effects, raise the complexity of the material's response to mechanical loading. Moreover, sophisticated test setups and additional control parameters increase the number of

potential sources of error. Some of these complications can be overcome by following recommendations given in the respective high temperature testing standards. When considering superalloy single crystals, additional aspects need to be considered. First, specimens need to be machined from directionally solidified bars or slabs, which are subjected to a multiple step heat treatment. Specimen material is expensive and superalloy single crystals are difficult to machine. Due to their high strength, they also require test rigs, which can apply high forces. Moreover, single crystal superalloys are used to manufacture turbine blades, with small critical dimensions (wall thicknesses of a cooled blade: mm-range). The availability of material also plays a role. These aspects promote smaller specimen geometries. In case of single crystal superalloys crystallographic aspects are important. It is not uncommon that research is performed on uniaxial specimens with nominal $\langle 100 \rangle$ directions, where deviations from up to 15° can occur.^[5] This can lead to large scatter as has been recently shown for creep conditions.^[24] The three specimens shown in Figure 4 were all machined from precisely oriented bars or slabs, combining Laue orientation with electro discharge machining. Cutting out precisely oriented specimens from slightly misoriented bars or slabs results in a loss of material and also promotes smaller geometries. Regarding the tests considered in the present work, their complexity increases as: creep $<$ CSR $<$ out-of-phase TMF. In comparison with the other two methods, creep loading is relatively simple. When the load is applied, the load line straightens itself out, and, from this point of view, gripping is easy. In contrast, when approaching 1273 K in longer term tests, creep grips have to withstand longer times at high temperatures. The advantages of the miniature creep test technique used in the present work have been discussed in the literature and it has been shown that displacements can be measured with sufficient accuracy outside of the gauge length,^[49] Figure 3b. This miniature creep test geometry cannot be used for CSR and OP-TMF testing, which also apply mechanical tensile loads. However, in CSR testing, constant strain rates are imposed and this requires precise measurement of strains. In the present work, this is done by ceramic rod-based extensometers, Figure 3a. These need to access the specimen and therefore a higher gauge length is required. In OP-TMF testing, where tensile and compressive loads are applied in strain control, the grip sections of the specimen need to be larger to allow for strong gripping, which is required to maintain the alignment of the specimens when changing from tensile to compressive loading. Moreover, the specimens need to be thicker than in the case of CSR testing, in order to avoid buckling.

4.2. CSR and Creep Behavior

In the present work, we compare three types of tests, which play a key role in material development and component design of single crystal Ni-base superalloys. High temperature constant strain rate tests provide apparent yield stresses $R_{p0.2}$. In the early stages of deformation, the stress–strain curves yield a straight line, from which an apparent elastic modulus can be derived. However, as shown in Figure 5a this apparent elastic modulus of 61 GPa is smaller than the value of 98 GPa, measured by Demtröder et al.^[53] who used resonant ultrasound spectroscopy (RUS).

This is not only because CSR tests are not optimized for measuring elastic moduli. It also reflects the fact that microscopic creep processes already occur in the apparent elastic regime of a high temperature CSR stress–strain curve. At lower temperatures, CSR tests show an increase of $R_{p0.2}$ with increasing temperature. SX can show this property, because they contain a high volume fraction of ordered γ' -phase. YSA is a well-known high temperature mechanical property of intermetallic phases, which is associated with dislocation cross slip from octahedral planes to cube planes. This results in the formation of KW locks. These sessile dislocation configurations need to be thermally activated.^[54–56] Indeed, KW locks are observed after CSR loading, Figure 11a. In the same temperature regime, an increase of strength with increasing temperature is not observed under creep conditions, where microstructures evolve at much smaller deformation rates of the order of 10^{-7} s^{-1} . In the creep community, this creep range is referred to as low temperature high stress creep regime. The nucleation and propagation of planar faults, Figure 11b, characterizes low temperature and high stress creep of SXs and the associated elementary mechanisms have been described in the literature (e.g., refs. [46,57–59]). At higher temperatures, the apparent yield stresses $R_{p0.2}$ show a significant dependence on imposed deformation rates, Figure 6a. At lower imposed deformation rates there is more time for recovery resulting in lower apparent yield stresses $R_{p0.2}$. Moreover, at high temperature, CSR tests no longer show YSA but $R_{p0.2}$ values decrease with increasing temperature. The results presented in Figure 6 suggest that the elementary processes, which govern creep and CSR behavior at higher temperatures, are related. The strain rate/stress data pairs from CSR tests and creep tests can be represented within a narrow Norton plot interval, suggesting that there is some continuity of mechanisms and that CSR data can be extrapolated to lower strain rates and provide preliminary lower bound estimates for creep rates. The elementary deformation mechanisms which govern high temperature and low stress creep have been described in the literature.^[5,28–40] Recently, the role of the misfit between the γ - and γ' -phase has been discussed. The need to minimize the overall strain energy results in a constant spacing between the dislocations in dislocation networks of the type shown in Figure 11c. It has been suggested that knitting processes between dislocations in both phases govern high temperature and low stress creep.^[60] The microstructural features shown in the TEM micrograph of Figure 11c are in line with this new view.

4.3. TMF and Creep Behavior

It is a well-known fatigue phenomenon that specimens with rougher surfaces fail earlier than specimens with smooth surfaces, Figure 8a, 9a, and 10c. This is related to the fact that fatigue failure starts with crack initiation at the specimen surface and crack growth from the specimen surface into the material.^[61] This holds for the majority of metallic materials subjected to different kinds of fatigue loading and is well appreciated for superalloy single crystals.^[62–64] The present work has not identified the elementary mechanisms which govern TMF crack initiation. But it provides clear evidence for the fact that rougher specimen surfaces result in short cyclic TMF-lives, Figure 8a. The negative

effect of surface roughness on fatigue lives has not been often reported for OP-TMF conditions. Clearly, local stresses are elevated when surfaces are rough. When the original surface of the superalloy is rough, this will also affect the surface quality of the oxide, which grows during the compression/heating part of the cycle. The oxide inherits the surface roughness of the specimen prior to OP-TMF exposure. Stresses acting on this scale during the tension/cooling loading ramp will have more influence in promoting cracking of the scale. Oxide scale crack nucleation will occur more readily when the surface is rougher. This qualitatively explains our findings. However, to reveal the physical nature of OP-TMF crack initiation, further work is required.

It is also well accepted that plastic deformation during fatigue is of a localized nature. The phenomenon of cyclic strain localization in persistent slip bands (PSBs) and models of the formation of extrusions and intrusions, which initiate microcracks have been discussed in detail (e.g., ref. [65]). Shear bands after fatigue loading have also been observed after thermomechanical fatigue loading in Ni-base SX.^[19,51] However, the low temperature mechanisms, where the formation of extrusion precedes crack nucleation does not hold for high temperature fatigue of superalloys. It is also well-known that oxidation plays a major role in high temperature fatigue,^[66–69] which is in line with the SEM micrograph in Figure 9b. TMF and creep impact materials differently. While fatigue is associated with localized cyclic deformation and surface crack initiation and growth, climb controlled creep represents a homogeneous deformation distributed throughout the microstructure and is associated with the evolution of internal damage. In polycrystalline engineering materials, the nucleation and growth of cavities on grain boundaries perpendicular to the direction of the maximum principal stress is a well-known example of such damage.^[70–72] Microstructural coarsening, evolution of the dislocation substructure and creep cavitation can explain tertiary creep in steels. Tertiary creep in Ni-base SX, which do not contain grain boundaries, is more difficult to rationalize.^[73]

A previous study of creep damage accumulation has shown that for the alloy investigated in the present work, creep cavities can nucleate and grow in the high temperature low stress regime (1323 K, 160 MPa).^[74] They were observed to be significantly smaller than pre-existing cast pores, which appeared to be the locations where final rupture initiated.^[74] Under the creep conditions considered in the present work ($T_{\max} = 1223$ K) no creep cavities were observed before necking started. While the cyclic rupture life of a TMF test is significantly affected by surface quality, the creep behavior is not sensitive to surface quality, Figure 8b. This is due to the fact that fatigue life is governed by surface crack initiation while creep damage accumulates in the volume of a specimen.

In the early days of high temperature technology, emphasis was mainly placed on the static load-carrying capacity of a component, which, however, often failed by fatigue.^[75] Combined linear damage accumulation rules with two terms, accounting for the consumed creep and fatigue life fractions were proposed,^[76,77] which did not work very well. Microstructural research on creep/fatigue interaction started in the 1980s.^[78–82] Central elements of these studies were that cavities on boundaries can promote intergranular fatigue crack growth^[78,79] or that the localized deformation (slip bands and

dislocation pile ups) caused by cyclic plasticity can assist in cavity nucleation.^[80–82] During a tensile hold in a high temperature fatigue test, creep stress relaxation and microstructural softening can decrease the crack extension force, which drives a high temperature fatigue crack.^[83] Note, that all microstructural scenarios^[78–83] briefly highlighted in this section focus on the tensile part of the high temperature fatigue cycle.

In the present work, we observe a detrimental effect of slower heating rates in the compression part of the OP-TMF cycle, Figure 10. To explain this effect, we assume that an OP-TMF experiment starts with the compression part of the cycle, imposing decreasing mechanical strains up to -0.5% while the temperature increases. At faster compression heating rates, less irreversible compressive strain accumulates than at slower compression heating rates. In the subsequent tensile part of the cycle, mechanical strains increase up to $+0.5\%$. This requires a total strain with a larger elastic component. It is more difficult to pull back a specimen which has seen more irreversible compressive strain. This is the reason why slower compression heating results in higher σ_{\max} -values leading to higher crack propagation rates and thus shorter cyclic lives, Figure 7 and 10. This represents an indirect creep effect, which shows that slower heating in the compressive part of the OP-TMF cycle results in dynamic recovery (dislocation annihilation occurs during high temperature deformation), which is associated with lower compressive peak stresses. It is interesting to compare the results of the present work with previous studies, where strain-controlled compression holds were shown to also shorten OP-TMF lives. Recovery in this type of tests is of a static nature (dislocation annihilation occurs in the absence of the accumulation of macroscopic plastic strain) and stress relaxation occurs during these compression holds.^[19] Strain-controlled compression holds at the maximum temperature of an OP-TMF cycle also result in a shortening of cyclic lives, consistent with the results obtained in the present study. Shortening of OP-TMF rupture lives by strain-controlled compressive holds at the maximum temperature was reported in two recent publications for polycrystalline Ni-base superalloys^[84,85] (Inconel 713LC, 773–1173 K, $\pm 0.3\%$, compression hold time: 600 s;^[84] DS alloy of CM 247LC type, 723–1123 K, ± 0.55 – 0.8% , compression hold time: 300 s^[85]). It had also been previously reported for the single crystal Ni-base superalloys TMS-75 and TMS-82+^[86] (673–1173 K, $\pm 1.28\%$ and $\pm 1.27\%$, hold time: 600 s) and for CMSX-4^[87] (673–1273 K, ± 0.7 – 1.1% , hold time: 300 s). All tests have in common, that recovery in the compressive high temperature part of an OP-TMF cycle relaxes stresses by transforming elastic into plastic strain. In strain-controlled testing, this requires higher stresses in the low temperature tensile part of the cycle. Lowering the minimum temperature has been shown to further reduce OP-TMF lives.^[87]

5. Summary and Conclusions

In the present work, the single crystal Ni-base superalloy ERBO/1 (CMSX-4 type) was subjected to high temperature constant strain rate (CSR), constant load tensile creep and out-of-phase thermomechanical fatigue (OP-TMF) testing. All tests were performed using precisely oriented [001] specimens, which were machined from directionally solidified and heat-treated

cylinders. Experiments were performed at temperatures between 1023 and 1223 K. The three tests considered in the present work are important standard tests in high temperature technology. For the alloy development, CSR testing can provide data for comparing alloys in the high temperature and low stress regime. CSR results from lower and medium temperatures must be handled with care. A YSA is exhibited which suggests that the strength of SX increases with temperature, which is not the case for creep conditions, and which does not play any role during OP-TMF testing. Creep tests are important for predicting the elongation of a turbine blade driven by centrifugal forces. OP-TMF tests must be performed, in order to account for the effect of thermal stresses associated with start-up and shut-down events. Creep deformation and damage mechanisms not only affect the tensile part of the OP-TMF cycle, but they also indirectly adversely affect OP-TMF life in compression as shown in the present work. From the experimental results obtained in the present study the following conclusions can be drawn: 1) In CSR testing (imposed deformation rate: $3.3 \times 10^{-4} \text{ s}^{-1}$) ERBO1 shows a yield stress anomaly (YSA), with a sharp stress maximum at 1073 K. While the strength observed in CSR testing increases up to this temperature, this does not hold for constant stress creep testing at much slower deformation rates. When increasing the temperature from 1043 to 1103 K, secondary creep rates increase from 2×10^{-8} to $3 \times 10^{-7} \text{ s}^{-1}$. The difference in typical strain rates used in CSR and creep testing is clearly of critical importance. 2) At higher temperatures, above the YSA peak, the strain rate/stress data pairs from CSR and creep tests fall into a narrow scatter band in a Norton plot which covers over eight orders of magnitude in strain rate. This suggests that the distinct difference in deformation mechanisms, which characterizes the material behavior in CSR and creep tests at lower temperatures, is not that pronounced at higher temperatures. 3) The stress strain hysteresis loops, which are recorded during OP-TMF cycling show no peculiarity when temperatures in the heating/compression part of the cycle pass through the temperature where the YSA maximum is observed during CSR testing. When passing through the YSA maximum the material's response is elastic and therefore elementary plastic deformation processes, which account for the YSA, do not affect the material's behavior. 4) The cyclic life of specimens subjected to OP-TMF test conditions is sensitive to the condition of the specimen surface, which minimum creep rates and creep rupture lives are not. Fatigue is generally associated with localized cyclic plastic deformation and surface crack initiation and growth, while creep represents a slow homogeneous deformation and shows non-localized microstructural softening. 5) High temperature oxidation is an important part of OP-TMF crack nucleation and growth. A reaction layer forms on the crack flanks of OP-TMF cracks, consisting of an outer oxide layer and an inner zone depleted of oxide forming elements. 6) An indirect creep effect during total mechanical strain-controlled OP-TMF testing was observed: Slower heating under OP-TMF conditions results in more inelastic compressive creep strain accumulation. In the following tensile part of the cycle, a higher stress is required to pull the specimen back to the maximum tensile strain. These higher tensile stresses increase crack propagation rates and thus lead to lower cyclic OP-TMF lives for slower heating rates.

Acknowledgements

All authors acknowledge funding through project A1 and A2 of the collaborative research center SFB/TR 103 funded by the Deutsche Forschungsgemeinschaft (DFG). M.J.M. acknowledges NSF DMREF Program under grant #1922239 and the Alexander von Humboldt program. A.D. acknowledges support from CSF under contract 20-11321S. Open Access funding enabled and organized by Projekt DEAL.

Conflict of Interest

The authors declare no conflict of interest.

Data Availability Statement

The data that support the findings of this study are available from the corresponding author upon reasonable request.

Keywords

constant strain rate testing, creep, out-of-phase thermomechanical fatigue, scanning and transmission electron microscopy, superalloy single crystals, surface quality

Received: February 13, 2024

Revised: May 13, 2024

Published online:

- [1] M. McLean, *Directionally Solidified Materials for High Temperature Service*, The Metals Society, London **1983**, ISBN 978-0-90435-752-3.
- [2] J. Lacaze, A. Hazotte, *Textures Microstruct.* **1990**, *13*, 1.
- [3] M. Durand-Charre, *The Microstructure of Superalloys*, Taylor & Francis Ltd., London **1998**, ISBN 978-90-5699-097-8.
- [4] M. J. Donachie, S. J. Donachie, *Superalloys: A Technical Guide*, 2nd ed., ASM International, Materials Park **2002**, ISBN 978-0-87170-749-9.
- [5] R. C. Reed, *The Superalloys: Fundamentals and Applications*, Cambridge University Press, Cambridge **2006**, ISBN 978-0-51154-128-5.
- [6] T. M. Pollock, S. Tin, *J. Propul. Power* **2006**, *22*, 361.
- [7] R. R. Jensen, J. K. Tien, *Metall. Trans. A* **1985**, *16*, 1049.
- [8] W. W. Milligan, S. D. Antolovich, *Metall. Trans. A* **1987**, *18*, 85.
- [9] D. Mukherji, H. Gabrisch, W. Chen, H. J. Fecht, R. P. Wahi, *Acta Mater.* **1997**, *45*, 3143.
- [10] X. Zhang, T. Jin, N. R. Zhao, Z. H. Wang, X. F. Sun, H. R. Guan, Z. Q. Hu, *Mater. Sci. Eng., A* **2008**, *492*, 364.
- [11] K. Hrutkay, D. Kaoumi, *Mater. Sci. Eng., A* **2014**, *599*, 196.
- [12] F. Garofalo, *Fundamentals of Creep and Creep-Rupture in Metals*, The Macmillan Company, London **1965**, ISBN 978-0-59840-248-6.
- [13] R. W. Evans, B. Wilshire, *Creep of Metals and Alloys*, Institute of Materials, London **1985**, ISBN 978-0-90435-759-2.
- [14] J. P. Poirier, *Ceramics and Minerals*, Cambridge University Press, New York, NY **1985**, ISBN 978-0-51156-445-1.
- [15] J. Cadek, *Creep in Metallic Materials*, Elsevier, Amsterdam **1988**, ISBN 978-0-44498-916-1.
- [16] M. Kassner, *Fundamentals of Creep in Metals and Alloys*, 3rd ed., Butterworth-Heinemann, Oxford **2015**, ISBN 978-0-08-099427-7.
- [17] H. Mughrabi, S. Kraft, M. Ott, *Superalloys* **1996**, *1996*, 335.
- [18] M. M. Shenoy, A. P. Gordon, D. L. McDowell, R. W. Neu, *J. Eng. Mater. Technol.* **2005**, *127*, 325.
- [19] J. J. Moverare, S. Johansson, R. C. Reed, *Acta Mater.* **2009**, *57*, 2266.

- [20] H. U. Hong, J. G. Kang, B. G. Choi, I. S. Kim, Y. S. Yoo, C. Y. Jo, *Int. J. Fatigue* **2011**, *33*, 1592.
- [21] S. Guth, S. Doll, K. H. Lang, *Mater. Sci. Eng., A* **2015**, *642*, 42.
- [22] R. Bürgel, H. J. Maier, T. Niendorf, *Handbuch Hochtemperatur-Werkstofftechnik*, 4th ed., Vieweg+Teubner Verlag, Wiesbaden **2011**, ISBN 978-3-8348-9907-1.
- [23] D. Goldschmidt, *Materialwiss. Werkstofftech.* **1994**, *25*, 311.
- [24] L. Heep, D. Bürger, C. Bonnekoh, P. Wollgramm, A. Dlouhy, G. Eggeler, *Scr. Mater.* **2022**, *207*, 114274.
- [25] J. K. Tien, S. M. Copley, *Metall. Trans.* **1971**, *2*, 215.
- [26] J. K. Tien, S. M. Copley, *Metall. Trans.* **1971**, *2*, 543.
- [27] A. Pineau, *Acta Mater.* **1976**, *24*, 559.
- [28] T. M. Pollock, A. S. Argon, *Acta Metall. Mater.* **1994**, *42*, 1859.
- [29] F. R. N. Nabarro, *Metall. Mater. Trans. A* **1996**, *27*, 513.
- [30] M. Véron, Y. Bréchet, F. Louchet, *Scr. Mater.* **1996**, *34*, 1883.
- [31] M. Véron, P. Bastie, *Acta Mater.* **1997**, *45*, 3277.
- [32] M. Kamaraj, C. Mayr, M. Kolbe, G. Eggeler, *Scr. Mater.* **1998**, *38*, 589.
- [33] M. Kamaraj, *Sadhana* **2003**, *28*, 115.
- [34] R. C. Reed, D. C. Cox, C. M. F. Rae, *Mater. Sci. Technol.* **2007**, *23*, 893.
- [35] A. Gaubert, Y. Le Bouar, A. Finel, *Philos. Mag.* **2010**, *90*, 375.
- [36] B. Fedelich, A. Epishin, T. Link, H. Klingelhöffer, G. Künecke, P. D. Portella, *Comput. Mater. Sci.* **2012**, *64*, 2.
- [37] L. Agudo Jácome, P. Nörtershäuser, J.-K. Heyer, A. Lahni, J. Frenzel, A. Dlouhy, C. Somsen, G. Eggeler, *Acta Mater.* **2013**, *61*, 2926.
- [38] L. Agudo Jácome, P. Nörtershäuser, C. Somsen, A. Dlouhy, G. Eggeler, *Acta Mater.* **2014**, *69*, 246.
- [39] L. Cao, P. Wollgramm, D. Bürger, A. Kostka, G. Cailletaud, G. Eggeler, *Acta Mater.* **2018**, *158*, 381.
- [40] L. Cao, D. Bürger, P. Wollgramm, K. Neuking, G. Eggeler, *Mater. Sci. Eng., A* **2018**, *712*, 223.
- [41] A. B. Parsa, P. Wollgramm, H. Buck, C. Somsen, A. Kostka, I. Povstugar, P. P. Choi, D. Raabe, A. Dlouhy, J. Mueller, E. Spiecker, K. Demtroeder, J. Schreuer, K. Neuking, G. Eggeler, *Adv. Eng. Mater.* **2015**, *17*, 216.
- [42] P. Hallensleben, H. Schaar, P. Thome, N. Jöns, A. Jafarizadeh, I. Steinbach, G. Eggeler, J. Frenzel, *Mater. Des.* **2017**, *128*, 98.
- [43] O. M. Horst, D. Adler, P. Git, H. Wang, J. Streitberger, M. Holtkamp, N. Jöns, R. F. Singer, C. Körner, G. Eggeler, *Mater. Des.* **2020**, *195*, 108976.
- [44] P. Thome, S. Medghalchi, J. Frenzel, J. Schreuer, G. Eggeler, *Ultramicroscopy* **2019**, *206*, 112817.
- [45] D. Whitehouse, *Surfaces and their Measurement*, Butterworth-Heinemann, Boston **2012**, ISBN 978-0-08097-201-5.
- [46] X. Wu, P. Wollgramm, C. Somsen, A. Dlouhy, A. Kostka, G. Eggeler, *Acta Mater.* **2016**, *112*, 242.
- [47] G. E. Dieter, *Mechanical Metallurgy*, McGraw-Hill, London **1988**, ISBN 978-0070168930.
- [48] A. B. Parsa, M. Sirrenberg, D. Bürger, M. J. Mills, A. Dlouhy, G. Eggeler, *Mater. Sci. Eng., A* **2024**, *899*, 146403.
- [49] P. Wollgramm, D. Bürger, A. B. Parsa, K. Neuking, G. Eggeler, *Mater. High Temp.* **2016**, *33*, 346.
- [50] D. Bürger, A. Dlouhy, K. Yoshimi, G. Eggeler, *Mater. Sci. Eng., A* **2020**, *795*, 139961.
- [51] M. Sirrenberg, D. Bürger, S. Guth, T. Babinsky, P. Thome, A. B. Parsa, G. Eggeler, *Mater. Sci. Eng., A*, unpublished.
- [52] B. Skrotzki, J. Olbricht, H.-J. Kühn, in *Handbook of Mechanics of Materials* (Eds: S. Schmauder, C. S. Chen, K. Chawla, N. Chawla, W. Chen, Y. Kagawa), Springer, Singapore **2019**, pp. 1917–1954, https://doi.org/10.1007/978-981-10-6884-3_44.
- [53] K. Demtröder, G. Eggeler, J. Schreuer, *Materialwiss. Werkstofftech.* **2015**, *46*, 563.
- [54] P. B. Hirsch, Y. Q. Sun, *Mater. Sci. Eng., A* **1993**, *164*, 395.
- [55] D. C. Chrzan, M. J. Mills, *Phys. Rev. B* **1994**, *50*, 30.
- [56] P. Veyssiere, *Mater. Sci. Eng., A* **2001**, *309*, 44.
- [57] X. Wu, A. Dlouhy, Y. M. Eggeler, E. Spiecker, A. Kostka, C. Somsen, G. Eggeler, *Acta Mater.* **2018**, *144*, 642.
- [58] L. Kovarik, R. R. Unocic, J. Li, M. J. Mills, *JOM* **2009**, *61*, 42.
- [59] V. A. Vorontsov, L. Kovarik, M. J. Mills, C. M. F. Rae, *Acta Mater.* **2012**, *60*, 4866.
- [60] A. B. Parsa, D. Bürger, T. M. Pollock, G. Eggeler, *Acta Mater.* **2024**, *264*, 119576.
- [61] S. Suresh, *Fatigue of Materials*, Cambridge University Press, Cambridge **1991**, <https://doi.org/10.1017/CBO9780511806575>.
- [62] A. Thakur, S. Gangopadhyay, *Int. J. Mach. Tools Manuf.* **2016**, *100*, 25.
- [63] D. Wu, D. Zhang, C. Yao, *Metals* **2018**, *8*, 549.
- [64] Z. R. Wu, S. Q. Wang, X. Yang, L. Pan, Y. D. Song, *J. Theor. Appl. Mech.* **2021**, *59*, 215.
- [65] H. Mughrabi, *Metall. Mater. Trans. A* **2009**, *40*, 1257.
- [66] J. Reuchet, L. Rémy, *Metall. Trans. A* **1983**, *14*, 141.
- [67] J. Reuchet, L. Rémy, *Mater. Sci. Eng.* **1983**, *58*, 19.
- [68] P. K. Wright, *ASTM STP* **1988**, *942*, 558.
- [69] A. Pineau, S. D. Antolovich, *Eng. Fail. Anal.* **2009**, *16*, 2668.
- [70] A. C. F. Cocks, M. F. Ashby, *Prog. Mater. Sci.* **1982**, *27*, 189.
- [71] H. Riedel, *Fracture at High Temperatures*, Springer, Berlin **1987**, ISBN 978-3-642-82963-5.
- [72] G. Eggeler, *Acta Metall. Mater.* **1991**, *39*, 221.
- [73] S. Sulzer, R. Reed, *Mater. Sci. Technol.* **2018**, *34*, 2174.
- [74] H. Buck, P. Wollgramm, A. B. Parsa, G. Eggeler, *Materialwiss. Werkstofftech.* **2015**, *46*, 577.
- [75] A. H. Meleka, *Metall. Rev.* **1962**, *7*, 43.
- [76] S. S. Manson, *Int. J. Fract.* **1966**, *2*, 327.
- [77] J. K. Wright, L. J. Carroll, S. Sham, N. Lybeck, R. N. Wright, in *ASME 2016 Pressure Vessels and Piping Conf.*, Vancouver, British Columbia **2016**, <https://doi.org/10.1115/PVP2016-63704>.
- [78] S. Baik, R. Raj, *Metall. Trans. A* **1982**, *13*, 1215.
- [79] J. K. S. Jadon, R. Singh, J. K. Mahato, *Mater. Today Proc.* **2022**, *62*, 5351.
- [80] B. F. Dyson, M. S. Loveday, M. J. Rodgers, *Proc. R. Soc. London, Ser. A* **1976**, *349*, 245.
- [81] M. H. Yoo, H. Trinkaus, *Acta Metall.* **1986**, *34*, 2381.
- [82] M. E. Kassner, T. A. Hayes, *Int. J. Plast.* **2003**, *19*, 1715.
- [83] S. Huang, J. Liu, J. Sheng, X. Meng, X. Hu, M. Zhu, J. Lu, J. Zhou, *Eng. Fract. Mech.* **2022**, *276*, 108922.
- [84] I. Sulák, K. Obrtlík, *Int. J. Fatigue* **2023**, *166*, 107238.
- [85] V. H. Dao, H. S. Yun, J. S. Koo, P. Jaeyeong, S. H. Nahm, *J. Alloys Compd.* **2024**, *990*, 174430.
- [86] H. Zhou, M. Osawa, H. Harada, T. Yokokawa, Y. Koizumi, T. Kobayashi, M. Waki, Y. Ro, I. Okada, *Superalloys* **2004**, *2004*, 225.
- [87] D. Arrell, M. Hasselqvist, C. Sommer, J. Moverare, *Superalloys* **2004**, *2004*, 291.